RSC Advances

PAPER

View Article Online
View Journal | View Issue

Cite this: *RSC Adv.*, 2023, **13**, 9046

Copper(II) and cobalt(III) Schiff base complexes with hydroxy anchors as sensitizers in dye-sensitized solar cells (DSSCs)†

Chiteri Gautam,[a] Devyani Srivastava,[a] Gabriele Kociok-Köhn,[b] Suresh W. Gosavi,[c] Vinod K. Sharma,[a] Ratna Chauhan,*[d] Dattatray J. Late,[e] Abhinav Kumar *[a] and Mohd. Muddassir[f]

Two Schiff base complexes of copper(II) and cobalt(III) having the formulae $[CuL_2]$ (**Cu-Sal**) and $[CoL_3]$ (**Co-Sal**) (HL = 2-(((2-hydroxyethyl)imino)methyl)phenol) have been synthesized and characterized microanalytically, spectroscopically and in the case of **Cu-Sal** using single crystal X-ray diffraction technique. The single crystal X-ray analysis reveals a square planar geometry around Cu(II) satisfied by phenoxide oxygen and imine nitrogen of the L^- ligand to generate a six membered chelate ring. The solid state structure of **Cu-Sal** is satisfied by varied intermolecular non-covalent interactions. The nature of these interactions has been addressed with the aid of Hirshfeld surface analysis. Both compounds have been used as sensitizers in TiO_2 based dye sensitized solar cells (DSSCs) and the DSSC experiments revealed that **Co-Sal** offers better photovoltaic performance in comparison to **Cu-Sal**. The **Co-Sal** exhibited a J_{sc} of 9.75 mA cm^{-2} with a V_{oc} of −0.648 V, incident photon to current conversion efficiency (IPCE) of 57% and η of 3.84%. The relatively better photovoltaic performance of **Co-Sal** could be attributed to better light absorption and dye loading than that of **Cu-Sal**.

Received 17th January 2023
Accepted 11th March 2023

DOI: 10.1039/d3ra00344b

rsc.li/rsc-advances

1 Introduction

During the past few decades, exponential growth in population and rapid industrialization have led to the decline in conventional non-renewable sources of energy.[1–5] Considering this and facing an energy crisis, several alternative renewable energy sources have to be searched and developed. Amongst several non-conventional sources of energy, dye-sensitized solar cells (DSSCs), sometimes regarded as third-generation photovoltaics, are gaining importance.[1–5] The increasing interest in this class of photovoltaic systems is due to their advantages such as simple fabrication processes in ambient conditions, semi-transparent and colorful appearances, possible plasticity, and high efficiencies.[6] The related power conversion efficiencies (PCEs) of various solar energy harvesting units continue to increase, targeting the Shockley–Queisser limit.[7,8] The efficiency of dye-sensitized solar cells (DSSCs) was improved significantly by Gratzel and O'Regan.[9] This impressive improvement in solar-to-electrical conversion efficiency has been achieved through device optimizations, use of transition metal redox couples in combination with suitable dyes, and low viscosity solvents, such as acetonitrile.[10–12] Due to direct conversion of sunlight-to-electrical energy, dye-sensitized solar cells (DSSCs) are relatively low-priced and highly-processable photovoltaic devices.[13–22] Their low cost and easy fabrication techniques can expand the commercialization and integration of these photovoltaic devices.[23] Hence, this next generation commercial solar cells are one of the most promising candidates and have attracted significant interest in this field.[24] Hence, from this viewpoint DSSCs can be the apt cost-efficient candidates with multifarious manufacturing possibilities and short energy-payback times.[25]

All DSSCs are comprised of five primary components: a counter electrode; a transparent electrode enabling photoexcitation of the dye; a photoexcitable dye; a conductive semiconductor, and one or more redox mediators.[26–46] Amongst all these components, the selection of a suitable photoexcitable dye plays a crucial role in deciding the overall photovoltaic

[a]*Department of Chemistry, Faculty of Science, University of Lucknow, Lucknow 226 007, India. E-mail: abhinavmarshal@gmail.com*

[b]*Material and Chemical Characterisation Facility (MC^2), University of Bath, Bath, BA27AY, UK*

[c]*Department of Physics, Faculty of Science, Savitribai Phule Pune University, Pune 411007, India*

[d]*Department of Environmental Science, Savitribai Phule Pune University, Pune 411007, India. E-mail: ratnasingh.bhu@gmail.com*

[e]*Centre for Nanoscience and Nanotechnology Amity University Maharashtra, Mumbai-Pune Expressway, Bhatan, Post Somatne, Panvel, Mumbai, Maharashtra 410206, India*

[f]*Department of Chemistry, College of Sciences, King Saud University, Riyadh 11451, Saudi Arabia*

† Electronic supplementary information (ESI) available. CCDC 2202408. For ESI and crystallographic data in CIF or other electronic format see DOI: https://doi.org/10.1039/d3ra00344b

performance of a DSSC set-up. Currently, varied coordination compounds especially ruthenium based N719, N3 dyes and their analogues have been used as possible sensitizers in DSSCs. Their selection can be accredited to their assorted metal-to-ligand charge transitions (MLCT), peculiar photo-excited stability and photo-physics.[26–46] Due to the high cost of ruthenium salts, researchers are in quest for other alternatives to develop economical and abundant metal complexes as sensitizers.[26–46] Amongst 3d transition series elements, Fe(II) ferrocene derivatives were found to behave like photosensitizer in DSSCs. In view of this, numerous homo- and heteroleptic complexes containing transition- or main group metal centers have been prepared using ferrocene-dithiocarbamates, dppf appended dithiolates and different heterocyclic ferrocene derivatives which were utilized in DSSCs.[47] Apart from ferrocene the applicability of other 3d transition series elements as sensitizers have been explored[26–46] amongst which the copper and cobalt based complexes have played a key role in uplifting the photovoltaic performance.

In our quest for new economical and higher performance sensitizers, we synthesized two Schiff base complexes of copper(II) and cobalt(III) *viz.* $[CuL_2]$ (**Cu-Sal**) and $[CoL_3]$ (**Co-Sal**) (HL = 2-(((2-hydroxyethyl)imino)methyl)phenol) and studied their use as sensitizers in DSSCs.

2 Experimental

2.1 Materials and methods

All synthetic procedures were carried out under ambient atmosphere. All solvents used for syntheses were distilled and dried prior to use by adopting standard methods. Fourier transform infra-red spectroscopy was performed using KBr discs on Shimadzu IR Affinity-1S spectrometer. ^{1}H and ^{13}C NMR spectroscopy were performed using Bruker Avance IIIHD NMR spectrometer using TMS as an internal standard. Microanalyses for both sensitizers were performed on a "Model CE-440 CHN analyser", while UV-Vis spectral data in methanol solution were collected on a SPECORD210 PLUS-BU. Mass spectrometry was performed using Bruker QTOF mass spectrometer.

2.2 Syntheses

2.2.1 Synthesis of the (*E*)-2-(((2-hydroxyethyl)imino) methyl)phenol. Salicylaldehyde (0.244 g, 2 mmol) and ethanolamine (0.123 g, mmol) were dissolved in 25 mL ethyl alcohol and refluxed for 6 h. After solvent removal the crude product obtained was isolated with dichloromethane (40 mL) and washed using diethyl ether. The dichloromethane fraction was dried using Na_2SO_4 (anhyd.) and filtered. An oily yellow substance of (*E*)-2-(((2-hydroxyethyl)imino)methyl)phenol (0.128 g, 1.586 mmol) was isolated after evaporation of dichloromethane.

2.2.1.1 Characterization data. Yellow oily solid. ^{1}H NMR (DMSO-d_6, 300 MHz, δ): 8.50 (s, 1H, CH=N), 7.67 (d, 1H, C_6H_4), 7.43 (m, 1H, C_6H_4), 7.19 (m, 1H, C_6H_4), 7.11 (d, 1H, C_6H_4), 2.81 (s, 4H, $-CH_2$). ^{13}C NMR (DMSO-d_6, 75.45 MHz, δ): 168.1, 162.1, 137.2, 123.8, 119.9, 118.1, 62.5, 58.2.

2.2.2 Synthesis of Cu-Sal. The ligand (*E*)-2-(((2-hydroxyethyl)imino)methyl)phenol (0.128 g, 1.586 mmol) was dissolved in methyl alcohol, and $Cu(CH_3COO)_2 \cdot H_2O$ (0.158 g, 0.793 mmol) was added in parts. The mixture was stirred for 4 h. The olive green precipitate was filtered, washed first with methyl alcohol (3 × 10 mL), then with diethyl ether (3 × 10 mL) and vacuum dried.

2.2.2.1 Characterization data. Olive green; yield 0.276 g, 70.58%; m.p. 172 °C; IR (KBr, cm^{-1}): 3328 (–OH), 1623 (C=N), 1476 ($-CH_2$) 2918 (Ar). Elemental analysis $C_{18}H_{20}CuN_2O_4$ (%): C, 55.16; H, 5.14; N, 7.15 found C, 55.82; H, 5.44; N, 7.45. ESI-MS: 389.0812 ($C_{18}H_{18}CuN_2O_4$).

2.2.3 Synthesis of complex Co-Sal. The oily substance of (*E*)-2-(((2-hydroxyethyl)imino)methyl)phenol (0.128 g, 1.5 mmol) was dissolved in methyl alcohol. Then $CoCl_2 \cdot 6H_2O$ (0.118 g, 0.5 mmol) was added in parts and the mixture was stirred for 4 h. The red brown precipitate was filtered, washed with methyl alcohol (3 × 10 mL), then with diethyl ether (3 × 10 mL) and vacuum dried.

2.2.3.1 Characterization data. Dark red-brown; yield 0.173 g, 62.90%; m.p. 80 °C; IR (KBr, cm^{-1}): 3352 (–OH), 1647 (C=N), 1442 ($-CH_2$). Elemental analysis $C_{27}H_{30}CoN_3O_6$ (%): C, 58.80; H, 5.48; N, 7.62. Found C, 59.18; H, 5.98; N, 7.93. ESI-MS 549.1467 ($C_{27}H_{30}CoN_3O_6$).

2.3 Crystallography

Intensity data for **Cu-Sal** were collected at 150(2) K on a Rigaku Xcalibur, EosS2 single crystal diffractometer using graphite monochromated Mo Kα radiation (λ = 0.71073 Å). Unit cell determination, data collection and data reduction were performed using the CrysAlisPro software.[48] The structures were solved with SHELXT and refined by a full-matrix least-squares procedure based on F^2 (SHELXL-2018/3).[49] All non-hydrogen atoms were refined anisotropically. Hydrogen atoms were placed onto calculated positions and refined using a riding model.

2.3.1 Crystal data for Cu-Sal. Empirical formula $C_{18}H_{20}CuN_2O_4$ M = 391.90 crystal system, monoclinic, $P2_1/c$, a = 18.2551(9) Å, b = 4.7699(2) Å, c = 19.5922(9) Å, β = 98.785(5)°, V = 1685.98(14) Å^3, Z = 4, D_{calc} = 1.544 Mg m^{-3}, $F(000)$ = 812, crystal size 0.427 × 0.268 × 0.165 mm^3, reflections collected 13 625, independent reflections 3859 [R(int) = 0.0294], GOF 1.024, final R indices [$I > 2$sigma(I)] R_1 = 0.0330, wR_2 = 0.0752, R indices (all data) R_1 = 0.0480, wR_2 = 0.0826 largest diff. peak and hole 0.287 and −0.464 e Å^{-3} CCDC no. 2202408.

2.4 Fabrication of DSSCs

For sandwich assembly of the DSSC, FTO glass plates (*F*-doped SnO_2: purchased from Pilkington. Co. Ltd. 8 Ω/γ, cleaned in ethanol in an ultrasonic bath for 30 min) were used to prepare photo- and counter-electrodes. The TiO_2 thin films were prepared using the doctor-blade technique by applying a TiO_2 paste (Ti-Nanoxide T, Solaronix) onto the FTO substrate followed by calcination at 450 °C for 30 min. For the preparation of photo-anodes the annealed TiO_2 thin films (~6 μm) were

immersed into the **Co-Sal** and **Cu-Sal** dye solution (1 : 1 ratio of dichloromethane : ethanol solution of **Co-Sal** and **Cu-Sal** dyes) for 6 h, then washing them with dichloromethane followed by ethanol and drying at room temperature. The Pt-counter-electrodes were prepared by screen printing of Pt catalyst (Solaronix) onto FTO and then sintered at 400 °C for 30 min. For the sandwich cell assembly, the dye-adsorbed TiO_2 photo-electrodes and Pt counter-electrodes were stuck together in a face to face manner which is sealed from three sides by using a hot-melt sealant film (Solaronix) as a spacer between the electrodes by heating it at 80 °C. A drop of electrolytic solution (0.05 M iodine, 0.05 M LiI and 0.5 M 4-*tert*-butylpyridine in acetonitrile) is then placed on the remaining open side of the cell assembly which is driven inside the cell by capillary action. Finally, this side is closed with araldite. The external connections on both electrodes are made of copper wire, silver paste and araldite.

2.5 Characterization of DSSCs

The photoelectrochemical performance characteristics (short circuit current J_{sc} (mA cm^{-2}), open-circuit voltage V_{oc} (V), fill factor ff and overall conversion efficiency η) were measured under illumination with a 1000 W Xenon lamp (Oriel 91193) using a Kiethley Model 2400. The light intensity was confirmed to be homogenous over an 8 × 8 $inch^2$ area by calibration with a Si solar cell for 1 sun light intensity (AM 1.5G, 100 mW cm^{-2}). Accidental increase of temperature inside the cell was prevented by using an electric fan. Incident photon-to-current conversion efficiency (IPCE) for the dyes were measured as a function of wavelength from 400–700 nm (PV measurement Inc.) using a standard tungsten-halogen lamp as monochromatic light and a broadband bias light for approximating 1 sun light intensity.

The electron transport properties were investigated using electrochemical impedance spectroscopy (EIS) with 10 mV alternative signal in the frequency range of 10^{-2} to 10^5 Hz and were performed on a CH 660C electrochemical analyzer (CH Instruments, Shanghai, China) with a two electrodes configuration. The photoanode was used as working electrode and the Pt electrode as counter electrode. The electron transport properties were investigated using electrochemical impedance spectroscopy (EIS) with 10 mV alternative signal in the frequency range of 10^{-2} to 10^5 Hz.

3 Results and discussion

3.1 Synthesis

The Cu(II) and Co(III) based sensitizers were synthesized by condensing salicylaldehyde and ethanolamine in equimolar ratio, which on reacting with Cu(II) and Co(II) in respective ratio in methanol yielded the corresponding complexes (Scheme 1). All these compounds were stable and characterized by micro-analyses, FT-IR, and in one case by single crystal X-ray diffraction.

The FTIR spectral data reveal that the bands at 3354 cm^{-1} and 3328 cm^{-1} signify the presence of hydroxyl groups in the **Co-Sal** and **Cu-Sal** complexes, respectively whereas the bands in the range of ~1620–1650 cm^{-1} are due to the –C=N (imine group) in both complexes.

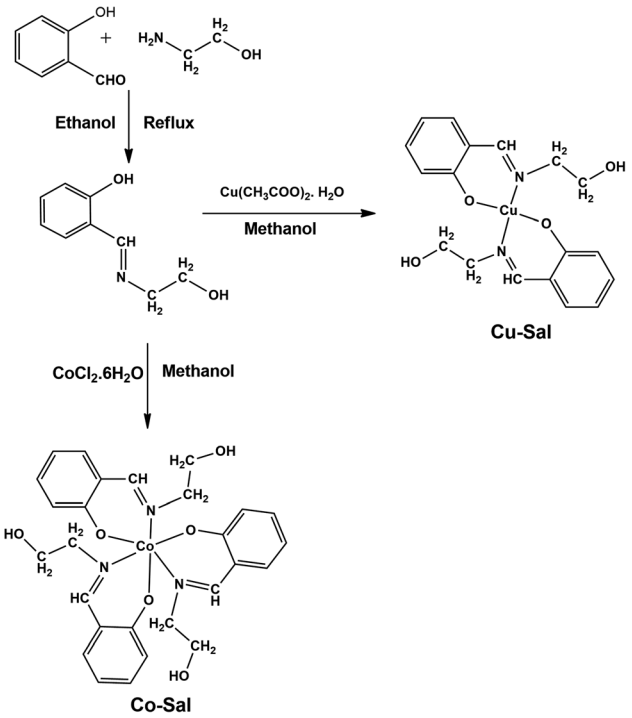

Scheme 1 Synthetic routes for the sensitizers.

3.2 Molecular structure and supramolecular architecture

The **Cu-Sal** crystallizes in the monoclinic space group $P2_1/c$ with two independent molecules in the unit cell. The immediate geometry around Cu(II) in **Cu-Sal** is square planar, which is defined by two phenolic oxygen centers O1 and O1′ and two imine nitrogen atoms N1 and N1′ of two 2-(((2-hydroxyethyl) imino)methyl)phenoxy (L^-) ligands. The two L^- ligands form six membered chelate rings and the Cu1 is present at the center of inversion in the centrosymmetric structure (Fig. 1). The Cu–O1 and Cu–N1 bond distances are 1.8778(14) and 2.0071(16) Å, respectively. The bite angle O(1)–Cu(1)–N(1) is 91.96(6), while the N(1)#1–Cu(1)–N(1) and O(1)–Cu(1)–O(1)#1 are exactly

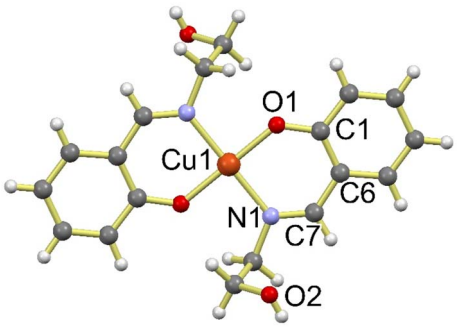

Fig. 1 Perspective view of the molecular geometry of **Cu-Sal**. Only one molecule present in the asymmetric unit is presented.

180.0°. Also, as evident from the structure, the alcoholic oxygen O2 remains protonated after complexation with the Cu(II).

The solid state framework of **Cu-Sal** is stabilized by several interactions amongst which the most important interaction is the O4–H4A···O2 intermolecular hydrogen bonding interaction that is operating between the two independent molecules comprising of the Cu1 and Cu2 centers in the asymmetric unit (Fig. 2). The O4–H4A···O2 interaction is 2.716 Å long with almost linear ∠O4–H4A···O2 169.74°, which indicates the strong nature of these hydrogen bonds. These hydrogen bonds propagate all along the three axes to generate a supramolecular coordination network (Fig. 2). In addition to the O–H···O interactions, **Cu-Sal** also forms weak intermolecular C–H···π interactions between aromatic C5–H5···C5 centers with an interaction distance of 2.727 Å and an angle of 169.75° to form a one-dimensional chain like framework (Fig. 3).

3.3 Hirshfeld surface analysis

The Hirshfeld surfaces[50–52] for **Cu-Sal** are shown in Fig. 4. The d_{norm} surfaces for the complex are mapped over a d_{norm} range of −0.5 to 1.5 Å. The weak non-covalent interactions discussed in the X-ray crystallography section summarize effectively as the deep red circular depressions in the d_{norm} surfaces indicating strong non-covalent interactions. The dominant O–H···O interactions are existing in Hirshfeld surface plots as the red shaded area. The small area and light colour on the surface represents weaker and C–H···π interactions.

Also, in the fingerprint plots[50–52] the complementary regions are shown, where one molecule acts as donor ($d_e > d_i$) and the other as acceptor ($d_e < d_i$) and have been decomposed to highlight particular atom-pair close contacts. In **Cu-Sal**, the O–H···O and C–H···π intermolecular interactions display distinct paired spike feature in their respective decomposed 2D fingerprint plots. The O–H···O interaction appears in the region of 0.6 Å < ($d_e + d_i$) < 2.4 Å with 11.2% contribution as light sky-blue pattern in full fingerprint 2D plots, while the C–H···π intermolecular interaction appears between 1.1 Å < ($d_e + d_i$) < 2.3 Å with 25.5% contribution. In the shape index plot that is sensitive to small variation in molecular shape due to irregular deformation induced from neighbouring crystalline environment, also indicates the mode of packing operating in the crystal. The surface of the shape index plot consists of several grooves and bumps and were constructed between −1 to 1. The reddish yellow hollow sections on the shape index plot governs the strong interactions in the crystal and is under the strong influence of the neighbouring environment, which is involved in supramolecular interaction. Apart from this, the bump like regions justified weak interactions or interactions least affected by the neighbouring crystalline environment in both compounds (Fig. 4). The surface curvedness, which is regarded as the function of RMS curvature of the surface has also been constructed for both cluster compounds. A closer inspection of the surface in **Cu-Sal** indicated yellow patches within the flat green surfaces. That reveals the isoenergetic supramolecular

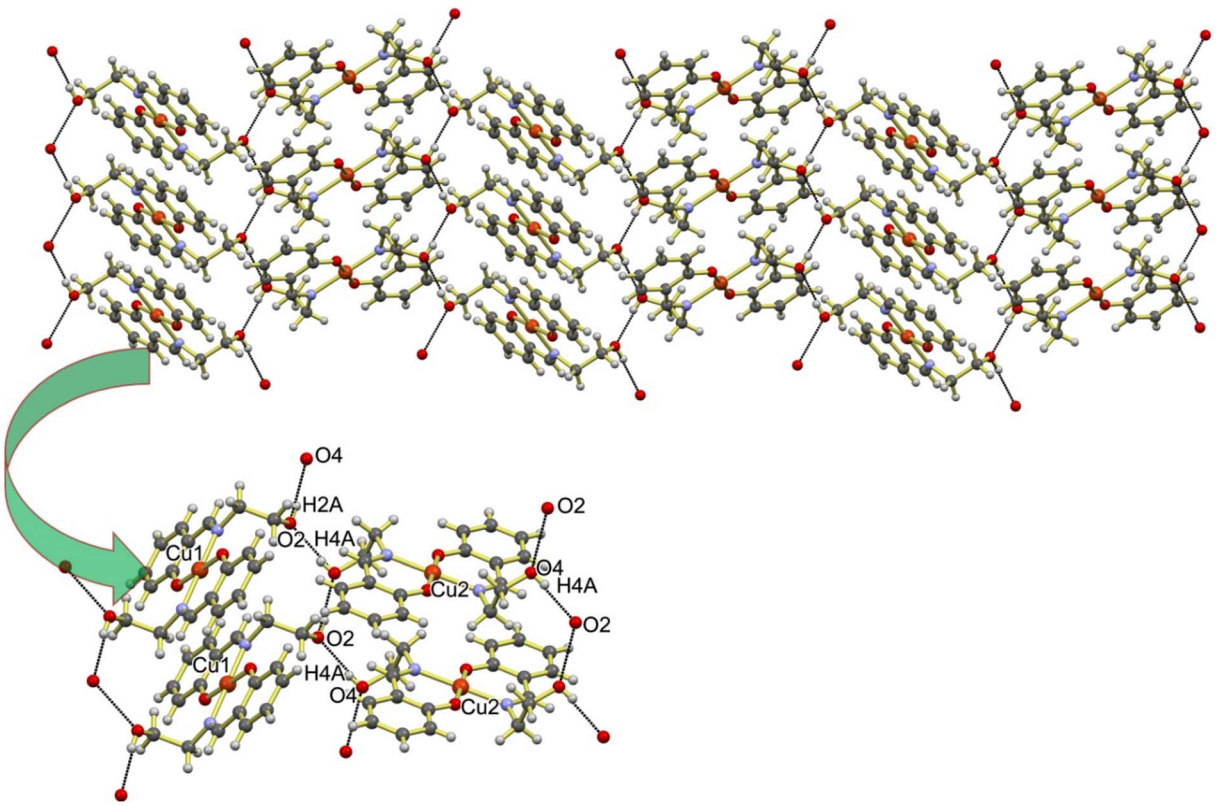

Fig. 2 Supramolecular architecture of **Cu-Sal** stabilized by intermolecular H–O···H hydrogen bonding interactions.

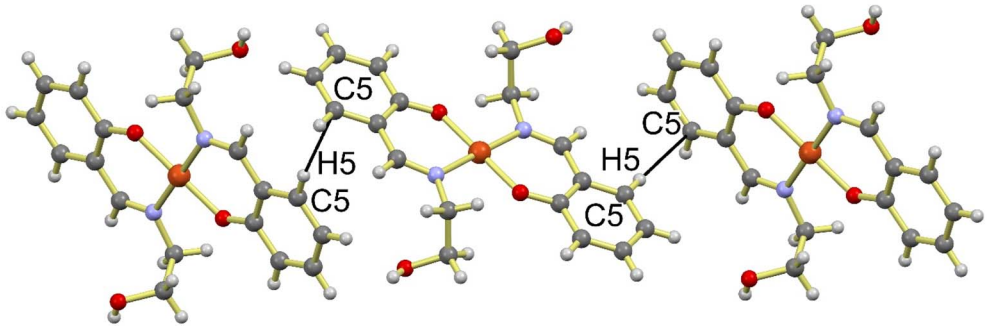

Fig. 3 The 1D chain formed by C–H···π interactions.

interactions in **Cu-Sal** (Fig. 4). For both compounds the crystal lattice void space has been assessed with standard void cluster parameter "unit cell + 5.0 Å" (Fig. 4). In the **Cu-Sal** lattice the void volume was 159.10 Å^3 with a void area of 596.16 Å^2 with asphericity and globular indices of 0.238 and 0.209 units, respectively. The larger magnitude of the void volume is a feature of the presence of weak non-covalent interactions in the single crystal supramolecular architecture. Also, the smaller globular index indicates that the supramolecular architecture in **Cu-Sal** is built-up by weak non-covalent interactions.

3.4 Optical properties

Fig. 5 presents the UV-vis absorption spectra for **Co-Sal** and **Cu-Sal** recorded in dichloromethane which display absorption bands in the visible range between 400–900 nm which arises because of the d–d transition. For **Cu-Sal** an absorption band appear from 450 to 550 nm in visible region, whereas for **Co-Sal** a broad band between 400–750 nm can be observed. The spectral response of **Co-Sal** reveals its superior light-harvesting ability. Both complexes display bands in the visible region,

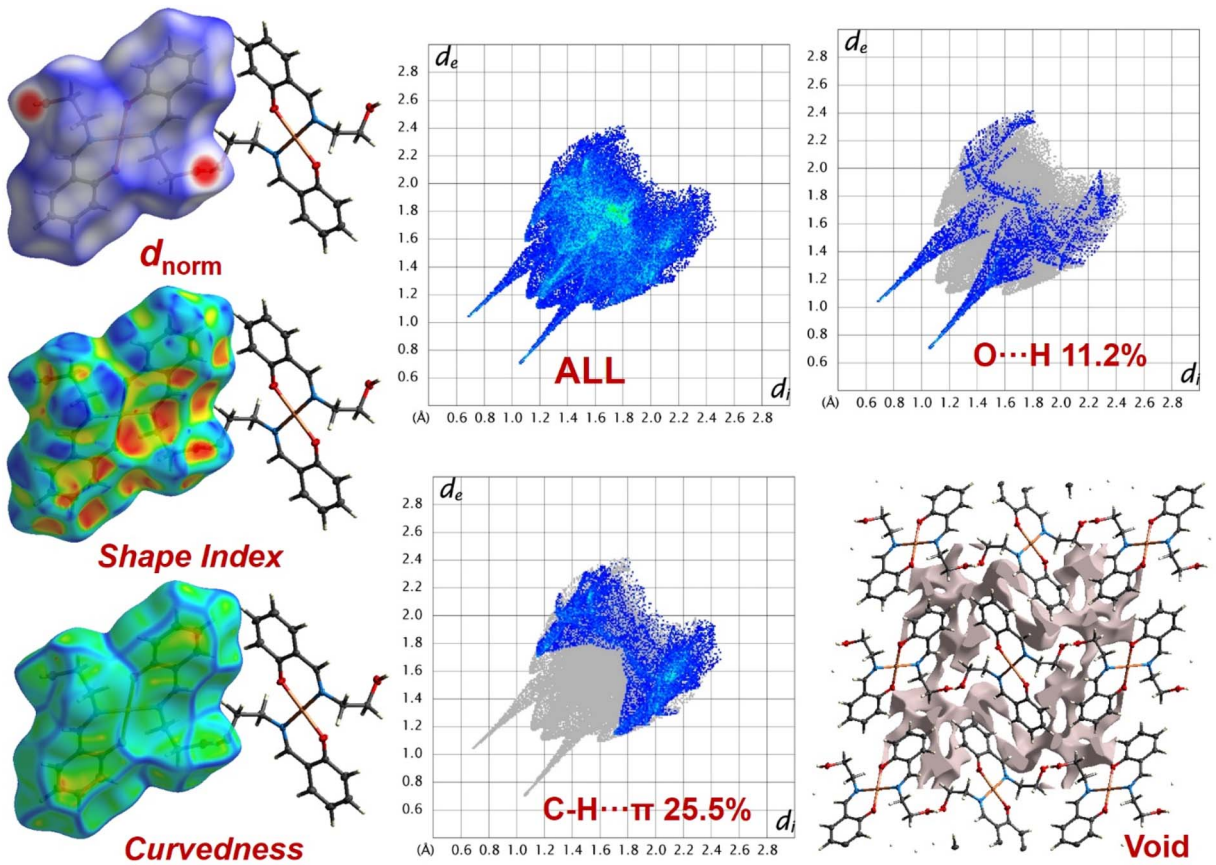

Fig. 4 Results of the Hirshfeld surface analyses for **Cu-Sal**, the left panel represents d_{norm}, shape index and curvedness; the central panel displays total and decomposed fingerprint plots and the right panel shows the results of crystal void calculations as well as a partial fingerprint plot.

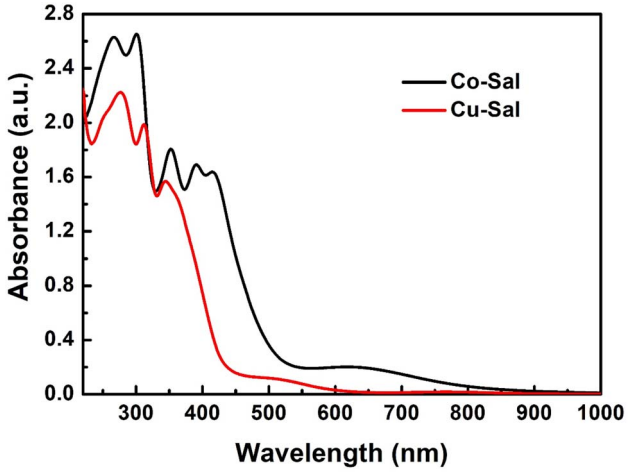

Fig. 5 Electronic absorption spectra for the sensitizers recorded in 1×10^{-4} M dichloromethane solutions.

therefore they can be utilized as sensitizers in dye-sensitized solar cells.

3.5 Photovoltaic performance of DSSCs

The photovoltaic properties of these dyes were studied by fabricating the DSSCs under identical conditions. The subsequent photovoltaic parameters are listed in Table 1, calculated *J–V* curves of the DSSCs are shown in Fig. 6a. From the data it can be concluded that the highest PCE for the sensitization of the dyes in DSSC based on **Co-Sal** is 3.84%, with a V_{oc} is 648 mV, J_{sc} is 9.75 mA cm^{-2}, and FF is 61%, while the PCE for the **Cu-Sal** sensitized cell is 3.00%. Evidently, the high PCE for the **Co-Sal** is the result of improved open-circuit voltage and short-circuit current. The enhanced performance for **Co-Sal** is due to its better electron donation properties along with better light-harvesting ability in the visible region, which is favorable for improving the J_{sc} of the DSSCs. We calculated the incident photon-to-current conversion efficiency (IPCE) spectra of the DSSCs to evaluate a collective measure of light harvesting, charge separation and charge collection efficiency. From Fig. 6b it can be concluded that the IPCE curve has a photocurrent response range of about 500 to 600 nm for **Co-Sal** whereas it is 400 to 500 nm for the Cu complexes. The IPCE values for **Co-Sal** and **Cu-Sal** complexes are 57% and 51% respectively and the percentage IPCE plot shows that the response range of photocurrent is steady with the absorption spectrum of the respective dye. The maximum electronic absorption intensity in **Co-Sal** can be observed in visible region at 450 nm and 610 nm, after that absorption intensity starts declining. In the IPCE for **Cu-Sal**, the onset starts from 400 nm and ends at 700 nm, whereas in the IPCE spectrum for **Co-Sal**, the onset commence from 450 nm and ends at 750 nm. Also, there are a broad shoulder in IPCE spectra for the dyes in visible range. As compared to the absorption spectra, in **Co-Sal** the shoulder was shifted to the shorter wavelength, which is suggesting some agglomeration of dyes on TiO_2 film. The broader IPCE spectra for both dyes suggest that dye sensitized DSSCs have a better competence in harvesting light as the absorption and IPCE spectra covered a wider wavelength range.

Table 1 presents DSSC performances of previously reported analogous sensitizers comprising.[52–55] The photovoltaic data suggested that performance of sensitizers investigated in presented study are comparable to the reported analogous sensitizers. However, the cell performance of the sensitizers are relatively inferior to that of the state of the art N719 dye,[52] which partly may be attributed to the relatively poor spectral response and inferior photo-electron transfer. However, as compared to the Ru(II)-based N719 sensitizers the sensitizers investigated herein are easy to synthesize and cost effective. Hence, to avail better cell performance, sensitizers should exhibit panchromatic spectral response, better sensitizer anchorage and efficient photo-electron transfer to the conduction band of semiconductor.

3.5.1 X-ray photoelectron spectroscopy. Further the mode of adsorption of best performing sensitizer **Co-Sal** at TiO_2 nanoparticulate, the XPS spectra of bare TiO_2 and **Co-Sal**@TiO_2 were recorded (Fig. S1†). This is because, XPS is highly surface sensitive technique to distinguish between different chemical states of the same atom. The XPS spectra of Ti 2p is shown in Fig. S2,† which indicates the splitting due to spin–orbit coupling for TiO_2 and **Co-Sal**@TiO_2. In TiO_2, The Ti 2p peaks observed at 458.67 eV and 464.52 eV are attributable to Ti^{4+} $2p_{3/2}$ and Ti^{4+} $2p_{1/2}$ states, respectively. This suggests that the surface of TiO_2 electrodes comprise of titanium(IV) dioxide only and suboxides *i.e.*, TiO, Ti_2O_3 *etc.* are not present.[56] In case of **Co-Sal**@TiO_2, these Ti 2p peaks shifted to slightly higher binding

Table 1 The DSSC performances of the sensitizers reported in this work and some previously reported analogous sensitizers

Sensitizers	J_{sc} (mA cm^{-2})	V_{oc} (V)	FF	η (%)	IPCE (%)	Ref.
Co-Sal	9.75	−0.648	0.61	3.84	57	This work
Cu-Sal	7.84	−0.632	0.60	3.00	51	
N719	8.85 ± 0.07	0.734 ± 0.02	0.64 ± 0.02	4.20 ± 0.05	55 ± 2	52
Zn-Fc	6.08 ± 0.03	0.684 ± 0.02	0.67 ± 0.02	2.79 ± 0.03	52 ± 2	52
Cd-Fc	5.13 ± 0.04	0.664 ± 0.02	0.67 ± 0.01	2.30 ± 0.04	50 ± 1	52
Hg-Fc	4.44 ± 0.03	0.656 ± 0.03	0.66 ± 0.01	1.95 ± 0.03	48 ± 1	52
RNPDA	7.12	0.79	—	3.42	—	53
PZn(Q)$_2$-C	2.52	0.745	0.586	1.11	—	54
PNi(Q)$_2$-C	1.27	0.650	0.550	0.45	—	54
Ni	2.23	0.61	0.52	0.71	—	55

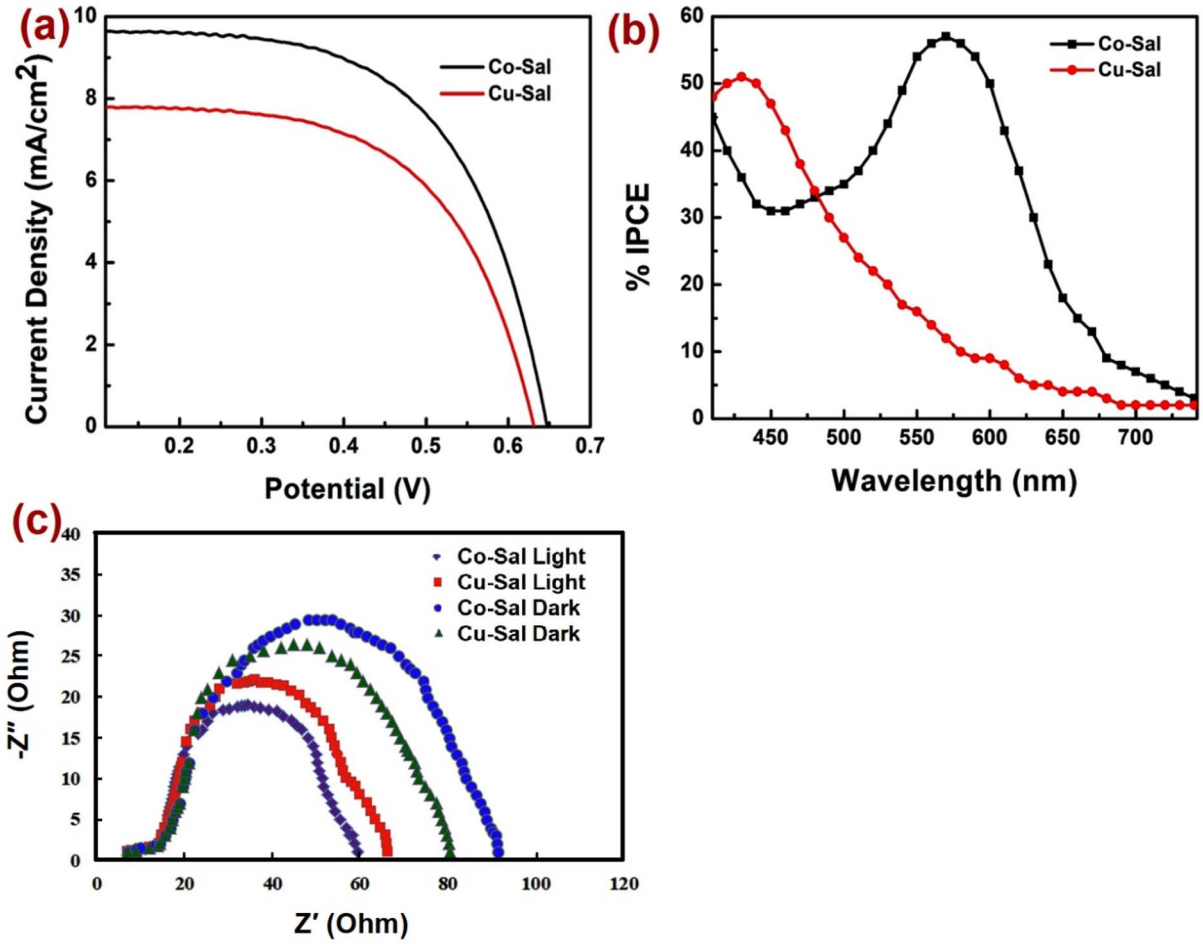

Fig. 6 (a) Current density–potential curves; (b) incident photo to current conversion efficiency and (c) Nyquist plots for **Cu-Sal** and **Co-Sal**.

energies as compared to bare TiO_2. The shift to higher binding energies could be due to change in the surface dipole and/or change in the Fermi level position in the band gap as a result of bonding of dye molecule with TiO_2 surface. In addition to the shift in B.E., a decrease in intensity of Ti 2p peaks is also observed indicating physio-chemical adsorption of dye ions on TiO_2 surface. Also, the O 1s spectra can provide information about the bonding interaction and surface geometrical structure of the anchoring group. The O 1s XPS spectra of dye sensitized TiO_2 and bare TiO_2 are shown in Fig. S3.† For the O 1s XPS spectra of dyes sensitized TiO_2, there is a shift of ~0.32 eV to lower binding energy in comparison to the non-sensitised O 1s TiO_2 spectra. In bare TiO_2, the bulk oxygen appeared at 531.3 eV and surface Ti···OH groups arises at 533.9 eV. For **Co-Sal**@TiO_2, the bulk oxygen is observed at 530.4 eV,[57,58] and the peak at 533.9 eV converts into the slight hump with shifting of peaks towards lower binding energy corresponding to the interaction of –OH group of dyes with surface Ti···OH, –Ti and –O of TiO_2.[59]

3.6 Electrochemical impedance spectra (EIS)

Electrochemical impedance spectroscopy was performed to measure the kinetics of the electron transport properties and charge recombination (Fig. 6c). The Nyquist plots of sensitized and co-sensitized photoelectrodes were recorded under standard global AM 1.5 solar irradiation in light and under dark by applying at their open circuit a potential (OCP) over a frequency range of 10^{-2} to 10^{5} Hz. In the EIS study, the semicircle in the middle frequency region is associated with the electron/charge transfer at the TiO_2/dye/electrolyte interface.[60] Figures show the Nyquist plots for DSSCs fabricated by using the **Co-Sal** and **Cu-Sal** in the dark and in the light respectively. Under light illumination, the two semicircles located in the high and middle frequency regions are attributed to the electrochemical reaction at the Pt/electrolyte interface and charge transfer at the TiO_2/dye/electrolyte interface. The semicircle of the large radius positioned at the middle frequency regions in the Nyquist plots decreases more with the **Co-Sal** than with the **Cu-Sal** in the light, showing less charge recombination and a high charge transfer rate for the **Co-Sal**. The radius of the semicircle in the light and in the dark are in the order of **Co-Sal** < **Cu-Sal** and **Co-Sal** > **Cu-Sal** respectively, which signify a decreasing trend of the electron transfer impedance (R_{ct}) as well as an increase in the charge transfer rate at this interface after sensitization.[61] The EIS study under light and dark conditions confirms that the charge transfer rate increases and the charge recombination rate

decreases after sensitization, which is favorable for enhancing the performance of DSSCs. Hence, overall, it could be concluded that the better photovoltaic performances of these sensitizers could be attributed to the presence of appropriate redox active center, ICT/MLCT moiety and apt anchoring groups, which provides the appropriate orientation of dyes on photoanode surface for its greater adsorption, greater electron lifetime and less recombination or delay in recombination at interfaces.[62]

4 Conclusion

In the investigation presented herewith, two Schiff base complexes of copper(II) and cobalt(III) have been synthesized using 2-(((2-hydroxyethyl)imino)methyl)phenol and for the copper complex the single crystal X-ray analysis revealed square planar geometry around Cu(II) satisfied by phenoxide oxygen and imine nitrogen of the 2-(((2-hydroxyethyl)imino)methyl) phenoxide ligand. The complex displayed varied intermolecular non-covalent interactions the nature of which has been addressed with the aid of Hirshfeld surface analysis. Both complexes were used as sensitizers in TiO_2 based dye sensitized solar cells (DSSCs) with the cobalt complex exhibiting better photovoltaic performance in comparison to the copper complex. The relatively better photovoltaic performance of the cobalt complex relates to better light absorption properties than these of the copper complex. This investigation will pave a new pathway to develop new imine-based sensitizers which will improve the DSSC performance.

Conflicts of interest

There are no conflicts to declare.

Acknowledgements

Dr Mohd. Muddassir is grateful to Researchers Supporting Project Number (RSP2023R141), King Saud University, Riyadh, Saudi Arabia, for financial assistance.

References

1 M. Nicole, B. Matteo, F. Lucia, B. Nadia, G. Claudio, B. Federico and B. Claudia, *Green Chem.*, 2020, **22**, 7168–7218.
2 A. M. Hisham, B. Vikas and K. B. Sanjay, *Renewable Sustainable Energy Rev.*, 2020, **121**, 109678.
3 M. Mrinalini, N. Islavath, S. Prasanthkumar and L. Giribabu, *Chem. Rec.*, 2019, **19**, 661–674.
4 G. Jiawei, K. Sumathy, Q. Qiquano and Z. Zhengping, *Renewable Sustainable Energy Rev.*, 2017, **68**, 234–246.
5 L. Giribabu, R. K. Kanaparthi and V. Velkannan, *Chem. Rec.*, 2012, **12**, 306–328; B. O'Regan and M. Gratzel, *Nature*, 1991, **353**, 737–740.
6 C. P. Lee, C. T. Li and K. C. Ho, *Mater. Today*, 2017, **20**, 267–283.
7 M. A. Green, Y. Hishikawa, W. Warta, E. D. Dunlop, D. H. Levi, J. Hohl-Ebinger and A. W. H. Ho-Baillie, *Prog. Photovoltaics*, 2017, **25**, 668–676.
8 M. A. Green and S. P. Bremner, *Nat. Mater.*, 2017, **16**, 23–34.
9 B. O'Regan and M. Gratzel, *Nature*, 1991, **353**, 737–740.
10 K. Kakiage, Y. Aoyama, T. Yano, K. Oya, J. Fujisawa and M. Hanaya, *Chem. Commun.*, 2015, **51**, 15894–15897.
11 A. Yella, H. W. Lee, H. N. Tsao, C. Yi, A. K. Chandiran, M. K. Nazeeruddin, E. W. G. Diau, C. Y. Yeh, S. M. Zakeeruddin and M. Grätzel, *Science*, 2011, **334**, 629–634.
12 S. Mathew, A. Yella, P. Gao, R. Humphry-Baker, B. F. E. Curchod, N. Ashari-Astani, I. Tavernelli, U. Rothlisberger, M. K. Nazeeruddin and M. Grätzel, *Nat. Chem.*, 2014, **6**, 242–247.
13 A. Mishra, M. K. Fischer and P. Bauerle, *Angew. Chem., Int. Ed.*, 2009, **48**, 2474–2499.
14 A. Hagfeldt, G. Boschloo, L. Sun, L. Kloo and H. Pettersson, *Chem. Rev.*, 2010, **110**, 6595–6663.
15 T. W. Hamann and J. W. Ondersma, *Energy Environ. Sci.*, 2011, **4**, 370–381.
16 B. E. Hardin, H. J. Snaith and M. D. Mc Gehee, *Nat. Photonics*, 2012, **6**, 162–169.
17 S. Zhang, X. Yang, Y. Numata and L. Han, *Energy Environ. Sci.*, 2013, **6**, 1443–1464.
18 A. Fakharuddin, R. Jose, T. M. Brown, F. Fabregat-Santiago and J. Bisquert, *Energy Environ. Sci.*, 2014, **7**, 3952–3981.
19 Y. Wu, W. H. Zhu, S. M. Zakeeruddin and M. Gratzel, *ACS Appl. Mater. Interfaces*, 2015, **7**, 9307–9318.
20 A. Polman, M. Knight, E. C. Garnett, B. Ehrler and W. C. Sinke, *Science*, 2016, **352**, 307.
21 J. M. Cole, G. Pepe, O. K. Al Bahri and C. B. Cooper, *Chem. Rev.*, 2019, **119**, 7279–7327.
22 Y. Saygili, M. Stojanovic, N. Flores-Díaz, S. M. Zakeeruddin, N. Vlachopoulos, M. Grätzel and A. Hagfeldt, *Inorganics*, 2019, **7**, 30.
23 Y. Saygili, M. Stojanovic, H. Michaels, J. Tiepelt, J. Teuscher, A. Massaro, M. Pavone, F. Giordano, S. M. Zakeeruddin, G. Boschloo, J.-E. Moser, M. Grätzel, A. B. Muñoz-García, A. Hagfeldt and M. Freitag, *ACS Appl. Energy Mater.*, 2018, **1**, 4950–4962.
24 M. Gratzel, *Nature*, 2001, **414**, 338–344.
25 B. O'Regan and M. A. Gratzel, *Nature*, 1991, **353**, 737–740.
26 Y. Bai, Q. Yu, N. Cai, Y. Wang, M. Zhang and P. Wang, *Chem. Commun.*, 2011, **47**, 4376–4378.
27 B. Oregan and M. Gratzel, A Low-Cost, High-Efficiency Solar-Cell Based on Dye-Sensitized Colloidal TiO_2 Films, *Nature*, 1991, **353**, 737–740.
28 S. Hattori, Y. Wada, S. Yanagida and S. Fukuzumi, *J. Am. Chem. Soc.*, 2005, **127**, 9648–9654.
29 M. Brugnati, S. Caramori, S. Cazzanti, L. Marchini, R. Argazzi and C. A. Bignozzi, *Int. J. Photoenergy.*, 2007, **2007**, 80756.
30 J. Cong, D. Kinschel, Q. Daniel, M. Safdari, E. Gabrielsson, H. Chen, P. H. Svensson, L. Sun and L. Kloo, *J. Mater. Chem. A*, 2016, **4**, 14550–14554.

31 M. Freitag, F. Giordano, W. Yang, M. Pazoki, Y. Hao, B. Zietz, M. Grätzel, A. Hagfeldt and G. Boschloo, *J. Phys. Chem. C*, 2016, **120**, 9595–9603.
32 H. Michaels, I. Benesperi, T. Edvinsson, A. B. Muñoz-Garcia, M. Pavone, G. Boschloo and M. Freitag, *Inorganics*, 2018, **6**, 53.
33 E. C. Constable, A. H. Redondo, C. E. Housecroft, M. Neuburger and S. Schaffner, *Dalton Trans.*, 2009, 6634–6644.
34 M. Freitag, Q. Daniel, M. Pazoki, K. Sveinbjörnsson, J. Zhang, L. Sun, A. Hagfeldt and G. Boschloo, *Energy Environ. Sci.*, 2015, **8**, 2634–2637.
35 Y. Saygili, M. Söderberg, N. Pellet, F. Giordano, Y. Cao, A. B. Muñoz-García, S. M. Zakeeruddin, N. Vlachopoulos, M. Pavone, G. Boschloo, L. Kavan, J. E. Moser, M. Grätzel, A. Hagfeldt and M. Freitag, *J. Am. Chem. Soc.*, 2016, **138**, 15087–15096.
36 A. N. M. Green, E. Palomares, S. A. Haque, J. M. Kroon and J. R. Durrant, *J. Phys. Chem. B*, 2005, **109**, 12525–12533.
37 G. Boschloo and A. Hagfeldt, Characteristics of the Iodide/Triiodide Redox Mediator in Dye-Sensitized Solar Cells, *Acc. Chem. Res.*, 2009, **42**, 1819–1826.
38 H. Kusama, *J. Photochem. Photobiol., A*, 2019, **376**, 255–262.
39 V. Chakrapani, D. Baker and P. V. Kamat, *J. Am. Chem. Soc.*, 2011, **133**, 9607–9615.
40 C. Teng, X. Yang, C. Yuan, C. Li, R. Chen, H. Tian, S. Li, A. Hagfeldt and L. Sun, *Org. Lett.*, 2009, **11**, 5542–5545.
41 Z. S. Wang, K. Sayama and H. Sugihara, *J. Phys. Chem. B*, 2005, **109**, 22449–22455.
42 B. V. Bergeron, A. Marton, G. Oskam and G. J. Meyer, *J. Phys. Chem. B*, 2005, **109**, 937–943.
43 F. Pichot and B. A. Gregg, *J. Phys. Chem. B*, 1999, **104**, 6–10.
44 K. S. Srivishnu, S. P. kumar and L. Giribabu, *Mater. Adv.*, 2021, **2**, 1229–1247.
45 A. B. Muñoz-García, I. Benesperi, G. Boschloo, J. J. Concepcion, J. H. Delcamp, E. A. Gibson, G. J. Meyer, M. Pavone, H. Pettersson, A. Hagfeldt and M. Freitag, *Chem. Soc. Rev.*, 2021, **50**, 12450–12550.
46 Y. Saygili, M. Stojanovic, H. Michaels, J. Tiepelt, J. Teuscher, A. Massaro, M. Pavone, F. Giordano, S. M. Zakeeruddin, G. Boschloo, J.-E. Moser, M. Grätzel, A. B. Muñoz-García, A. Hagfeldt and M. Freitag, *ACS Appl. Energy Mater.*, 2018, **1**, 4950–4962.
47 (*a*) R. Chauhan, M. Trivedi, L. Bahadur and A. Kumar, *Chem.–Asian J.*, 2011, **6**, 1525–1532; (*b*) A. Singh, P. Singh, G. Kociok-Köhn, M. Trivedi, A. Kumar, R. Chauhan, S. B. Rane, C. Terashima, S. W. Gosavi and A. Fujishima, *New J. Chem.*, 2018, **42**, 9306–9316; (*c*) R. Chauhan, S. Auvinen, A. S. Aditya, M. Trivedi, R. Prasad, M. Alatalo, D. P. Amalnerkar and A. Kumar, *Sol. Energy*, 2014, **108**, 560–569; (*d*) R. Chauhan, M. Shahid, M. Trivedi, D. P. Amalnerkar and A. Kumar, *Eur. J. Inorg. Chem.*, 2015, 3700–3707; (*e*) R. Chauhan, R. Yadav, A. K. Singh, M. Trivedi, G. Kociok-Köhn, A. Kumar, S. Gosavi and S. Rane, *RSC Adv.*, 2016, **6**, 97664–97675; (*f*) R. Yadav, A. Singh, G. Kociok-Köhn, R. Chauhan, A. Kumar and S. Gosavi, *New J. Chem.*, 2017, **41**, 7312–7321; (*g*) R. Yadav, M. Trivedi, G. Kociok-Köhn, R. Chauhan, A. Kumar and S. W. Gosavi, *Eur. J. Inorg. Chem.*, 2016, **6**, 1013–1021.
48 *CrysAlisPro 1.171.41.122a*, Rigaku Oxford Diffraction, 2021.
49 G. M. Sheldrick, *Acta Crystallogr., Sect. C: Struct. Chem.*, 2015, **71**, 3–8.
50 (*a*) R. Yadav, M. Trivedi, G. Kociok-Köhn, R. Prasad and A. Kumar, *CrystEngComm*, 2015, **17**, 9175–9184; (*b*) A. Singh, A. Singh, D. Srivastava, G. Kociok-Köhn, R. D. Köhn, A. Kumar and M. Muddassir, *CrystEngComm*, 2022, **24**, 4274–4282; (*c*) P. Singh, A. Singh, A. Singh, A. K. Singh, G. Kociok-Köhn, A. Alowais, N. A. Y. Abduh, M. Muddassir and A. Kumar, *CrystEngComm*, 2020, **22**, 2049–2059.
51 (*a*) A. Kumar, A. Singh, R. Yadav, S. Singh, G. Kociok-Köhn and M. Trivedi, *Inorg. Chim. Acta*, 2018, **471**, 234–243; (*b*) R. Yadav, M. Trivedi, R. Chauhan, R. Prasad, G. Kociok-Köhn and A. Kumar, *Inorg. Chim. Acta*, 2016, **450**, 57–68.
52 C. Gautam, A. Singh, S. W. Gosavi, R. Chauhan, V. K. Sharma, A. Alarifi, M. Afzal, M. Muddassir and A. Kumar, *Appl. Organomet. Chem.*, 2022, **36**, e6608.
53 S. Kamalesu, A. A. Babu and K. Swarnalatha, *Inorg. Chem. Commun.*, 2019, **104**, 88–92.
54 J. Deng, L. Guo, Q. Xiu, L. Zhang, G. Wen and C. Zhong, *Mater. Chem. Phys.*, 2012, **133**, 452–458.
55 D. Kilinc, O. Sahin and S. Horoz, *J. Ovonic Res.*, 2018, **14**, 71–77.
56 K. E. Lee, M. A. Gomez, T. Regier, Y. Hu and G. P. Demopoulos, *J. Phys. Chem. C*, 2011, **115**, 5692–5707.
57 G. W. Simmons and B. C. Beard, *J. Phys. Chem.*, 1987, **91**, 1143.
58 M. Takagi-Kawai, M. Soma, T. Onishi and K. Tamaru, *Can. J. Chem.*, 1980, **58**, 2132.
59 G. Jin, R. Park, H. Park, J. Seo, S. Lee and M. Lee, *Chin. Med. J.*, 2010, **123**, 3132.
60 C. S. Chou, R.-Y. Yang, C.-K. Kuo and Y.-J. Lin, *Powder Technol.*, 2009, **194**, 95–105.
61 K. Matsumoto, N. Saito, T. Mitate, J. Hojo, M. Inada and H. Haneda, *Cryst. Growth Des.*, 2009, **9**, 5014.
62 (*a*) S. A. Miltsov, V. S. Karavan and V. A. Borin, *J. Gen. Chem.*, 2019, **89**, 1055–1057; (*b*) C. A. Goss and H. D. Abruŋa, *Inorg. Chem.*, 1985, **24**, 4263–4267; (*c*) L. Galucci, G. pampaloni, C. Pinzino and A. Prescimone, *Inorg. Chim. Acta*, 2006, **359**, 3274–3278.